LAWRENCE
LIVERMORE
NATIONAL
LABORATORY

UCRL-JRNL-213934

Surface Deformation Behavior of BSTOA Ti-6Al-4V during Laser Shock Processing

B. S. El-Dasher, T. M. Zaleski, J. J. Gray, S. J. Rybak, H.-L. Chen

July 22, 2005

Journal of Applied Physics

Disclaimer

Surface Deformation Behavior of BSTOA Ti-6Al-4V during Laser Shock Processing

Bassem S. El-Dasher, Tania M. Zaleski, Jeremy J. Gray,
Sergiusz J. Rybak, and Hao-Lin Chen

Lawrence Livermore National Laboratory, Livermore, CA 94550

The surface of a beta solution treated and overaged (BSTOA) Ti-6Al-4V alloy specimen deformed by laser shock processing was studied using electron backscatter diffraction (EBSD), scanning electron microscopy (SEM), and atomic force microscopy (AFM). Slip steps were observed within grains oriented with their c-axis nearly parallel to the specimen surface normal. Based on the slip step traces and orientation information, the slip planes were determined to be $\{11\bar{2}2\}$ for grains with their c-axis within 15° of the specimen surface normal and $\{11\bar{2}1\}$ for grains with their c-axis between 15° and 40° away from the specimen surface normal. Although both these planes are known to belong to twinning systems, $\{11\bar{2}2\}\langle 11\bar{2}\bar{3}\rangle$ and $\{11\bar{2}1\}\langle 11\bar{2}\bar{6}\rangle$ respectively, the latter has not been observed to operate as a slip system. Examination of the Taylor factors associated with these slip systems shows that the grains with slip steps have the lowest Taylor factors. Determination of localized lattice rotations showed a unique behavior in grains with slip steps, such that all the lattice rotations were concentrated about the steps, with almost no orientation variations in between slip steps. This distribution indicates that stress concentrations exist at the slip steps, which could potentially affect the performance of the material.

I. INTRODUCTION

The generation of shockwaves in solids using high intensity lasers was initially investigated three to four decades ago[1-7]. In contrast to laser melting techniques that rely on thermal processes (*i.e.* rapid solidification) [8-11], laser shock processing (LSP, also called laser shock peening) improves material properties through localized mechanical deformation by employing the shockwaves generated at the work-piece surface. This work-hardens the material at and near the surface and leaves a residual compressive stress extending up to 4 mm into the work-piece[12-14]. The shockwaves are generated through ablation of surface material, which is transformed into a plasma. This plasma moves away from the material surface at a high rate, consequently applying a pressure wave on the material surface which propagates in the form of a shockwave. The pressure created by the plasma generated at the specimen surface depends on the laser fluence used, as well as the presence of a plasma-confining tamping layer[15-19].

Evidence of microstructural changes was first observed in foils[6], which showed a marked increase in vacancy concentrations due to shockwave propagation. Later work in bulk aluminum specimens showed dense, tangled dislocation substructures and led to the reasoning that these were the source of the observed work-hardening[20]. Increased dislocation densities were observed in laser shocked copper[21,22] and deformation twinning was observed in laser shocked copper[22] and bcc metals[23]. In copper, the deformation mode was found to be dependent on the pressures generated at the surface such that pressures between 12 and 20 GPa yielded microstructures with a large number of dislocation cells and pressures between 40 and 60 GPa generated large amounts of micro-twins and laths[22].

The technological benefits of LSP have been demonstrated on numerous occasions. Application of LSP to components requiring improved stress corrosion cracking resistance, such as nuclear light water reactor shrouds, have shown marked corrosion performance improvements[24-26]. In components where improving fatigue strength is of critical importance, such as aircraft components, LSP has also been successfully applied[27-31]. In both types of applications, it is believed that the introduction of residual compressive stresses in the near surface region of the material aids by mitigating the onset and growth of cracks.

Despite the great amount of work performed to date on the performance of materials treated using LSP, how material anisotropy can play a role in the effectiveness of the process has yet to be considered.

While the extent of this role is dependent on many microstructural parameters, it is typically most dependant on grain size and texture (preferred grain orientations). While titanium alloys have been popular for specific applications in the aircraft industry for some time now, primarily due to their combination of high strength and light weight, beta solution treated and overaged (BSTOA) Ti-6Al-4V has been adopted as the material of choice for airframe members. Considering the costs involved in producing these airframe members, the application of LSP for fatigue life improvement is a sensible consideration.

In its BSTOA form, Ti-6Al-4V is primarily composed of the hexagonal close-packed (hcp) α-phase with some residual β-phase. A by-product of the BSTOA process is large grain sizes (~1mm diameter), especially if the solution treatment is performed for an extended period of time. Given that grains of this size are approaching typical spot sizes used for LSP (2-3mm), and that α titanium is known to be anisotropic[32], large differences in material response are possible in differently oriented grains. This in turn could translate into an inhomogeneous distribution of residual stresses in the material, thereby decreasing the effectiveness of the LSP process.

In this work the topography and crystallographic orientations of grains at the surface of a BSTOA Ti-6Al-4V specimen are studied before and after the laser shock process in order to determine the effect of the grain orientations (and hence anisotropy) on material behavior.

II. EXPERIMENTAL

A disc 44mm in diameter with a height of 15mm was cut from an ingot of BSTOA Ti-6Al-4V manufactured and solution treated in accordance with ASM Standard 4905. Wire electrical discharge machining was used in cutting the disc to minimize the amount of deformation introduced into the specimen. Since we were interested in studying the effects of LSP as a function of grain orientation, it was necessary to prepare the specimen prior to the LSP treatment. The specimen surface was metallographically prepared by grinding using silicon carbide paper down to 1200 grit, followed by a rough polish using 3µm diamond slurry and a final polish using 0.02µm colloidal silica. Two fiducial marks 14mm apart were created off-center for use as sample alignment markers during the remainder of the experiment.

Characterization of the polished specimen was performed using electron backscatter diffraction (EBSD) mapping[33,34]. This technique was employed as it is able to map large areas of microstructure while

yielding local crystallographic orientation information. The mapping was carried out using a TexSEM Laboratories OIM 4 system equipped with a Peltier cooled CCD camera attached to an FEI Company Quanta 200 environmental scanning electron microscope (ESEM). The specimen was tilted to 70^{o}, and an accelerating voltage of 30kVand a beam current of 98μA were used in spot mode. Data was collected on a square grid with a step size of 10μm, covering an area of 9.6mm by 5.7mm. This area is illustrated schematically in Figure 1.

Aluminum tape was then applied to the polished surface in preparation for the laser treatment and was used as the sacrificial ablation material for the plasma generation. This plasma generation was achieved using a Q-switched high power laser system that included a stimulated Brillouin scattering phase conjugation device to ensure a uniform energy distribution across the laser spot. The laser system was set to produce an irradiance of 12 GW/cm^2 with a pulse duration of 18 ns, with a square spot size of 3mm and an overlap of 30% between adjacent spots. Flowing water over the specimen surface provided the transparent tamping layer. A schematic of the experimental setup is shown in Figure 2.

Once the LSP process was completed, EBSD mapping was performed using the same parameters as before on the same specimen region characterized prior to the LSP treatment. To provide a topological map of the region, the specimen surface was imaged in the ESEM. A four-quadrant solid-state backscatter electron detector was used in the A-B mode, as this elucidated surface topography. 18 rows by 30 columns of images were acquired at a magnification of 800X and then stitched together to form a collage. Comparison between the EBSD map and the topography collage were used to determine small areas (approximately 100μm squares) of interest for further study.

In these smaller areas, the features of interest were also the crystallographic orientations and the surface topography. EBSD was again used for determination of local crystallographic orientations, although in these cases a step size of 0.75μm and a triangular grid were used. Atomic force microscopy (AFM) was used for the topographic mapping of these areas, and was performed in contact mode using a Digital Instruments Dimension 3100 with square scan areas of either 80 or 100μm a side.

III. RESULTS

In Figure 3, the results of the large area mapping are presented. Figure 3(a) shows the microstructure determined by EBSD, with the grain boundaries shown as black lines. It can be seen that the grain sizes vary between 300μm to 1.5mm. In Figure 3(b), the topography of the same area is presented. It is seen that specific areas show slip steps at the surface. The ten grains with the most prevalent slip steps were identified and numbered in Figure 3(a), and then examined using AFM and high resolution EBSD scans as mentioned previously.

Figure 4 shows the results of orientation and slip trace analysis on grain 2b. Figure 4(a) shows the surface map of grain 2, with the boxed area indicating the region scanned by AFM (Figure 4(b)).The AFM map allows us to obtain the slip trace normals. The slip trace analysis was performed by plotting the typically observed α-titanium slip plane normals, *i.e.* $(0001), \{10\bar{1}0\}, \{10\bar{1}1\}$, and $\{11\bar{2}2\}$, in a stereographic projection and overlaying the slip trace normals onto the projection (Figure 4(c)) in order to determine which of the slip system planes is active. Interestingly, none of the normal projections of the four typically observed slip planes intersected the slip trace normals. Instead, it was observed that the active slip planes are $\{11\bar{2}2\}$, which have been previously observed as twinning planes. In Figure 4(d), the three slip planes from the $\{11\bar{2}2\}$ family active in grain 2b are schematically shown.

In Figure 5, we repeat the slip trace analysis for grain 3b. In this grain, only two slip traces were observed. Again comparison to the typically observed α-titanium slip planes showed that none of them were active, and in this case the slip planes were determined to be $\{11\bar{2}1\}$. This analysis was performed for all ten grains, and the slip lanes were consistently determined to be either $\{11\bar{2}2\}$ or $\{11\bar{2}1\}$. Table I summarizes the results of the analyses for all ten grains.

To determine the role of crystallographic orientation on the observed slip planes, surface normal inverse pole figures were constructed using the average orientations of the grains in question, as determined using the quaternion method[35]. In Figure 6(a), the plane normals parallel to the specimen surface normal for all ten grains are plotted. It can be seen that the distribution is centered around the (0001) plane, with the furthest grain rotated away by approximately 40°. Figure 6(b) illustrates the same plane normal distribution, except it is restricted to only the grains with the $\{11\bar{2}2\}$ slip steps. It can be seen that the distribution is still

clustered around (0001), although the furthest grain is now only 15° away. It follows then that the distribution for the grains with $\{1\bar{1}21\}$slip steps, shown in Figure 6(c), illustrates that these grains are oriented between 15° and 40° away from the basal plane.

IV. DISCUSSION

In this section two interrelated topics will be addressed. The first relates to the identification of the active slip systems observed, and the role of the grain orientation in slip system selection. The second topic addresses the differences between the grains with and without slip steps at the micron scale in terms of lattice misrorientations, as well as the implications of these differences.

- Slip Systems and Orientation Dependence:

While the stereographic projection analyses performed in Figures 4 and 5 allows for the determination of the slip planes corresponding to the observed slip steps, it does not allow for the determination of the slip direction. To do this, it is necessary to determine the rotation of the lattice during deformation. Traditionally this requires the measurement of the grain orientation at three or four different deformation levels, and then subsequently determining the direction of lattice rotation. However due to the experimental restriction of LSP of only one deformation level, this type of determination is not possible. Instead, knowledge of the possible systems active on the determined slip planes is used.

In α titanium, $\{1\bar{1}22\}$ and $\{1\bar{1}21\}$ have only been observed to operate as twinning planes in deformation[36,37], such that the deformation twins are $\{1\bar{1}22\}\langle 11\bar{2}\bar{3}\rangle$ [38] and $\{1\bar{1}21\}\langle 11\bar{2}\bar{6}\rangle$ [39], respectively. The topography presented in Figure 3(b) suggests that deformation twinning may be taking place, since it can be seen that many grains have been deformed during the shock process but show no surface slip steps. Furthermore, examination of the EBSD orientation data shows very little lattice rotations within the same grains, indicating that the deformation occurs at a length scale smaller than that resolvable by the technique. Considering that previous work has shown that deformation twins are produced in other material due to LSP[22-23], we may assume that they also occur in our specimen.

This then raises two questions:

1. Can glissile slip occur on the $\{1\bar{1}22\}\langle 11\bar{2}\bar{3}\rangle$ and $\{1\bar{1}21\}\langle 11\bar{2}\bar{6}\rangle$ systems?

2. Why do the near <0001> grains deform on these slip systems?

To answer the first question, we look to the literature. Nearly forty years ago, Rosenbaum proposed a mechanism using a hard sphere model in which slip on the $\{11\bar{2}2\}$ planes and in the $\langle 11\bar{2}\bar{3}\rangle$ direction was geometrically possible if deformation occurred on twin-like stacking faults with displacements parallel to the slip direction[40]. However, a major difference between this mechanism and typical slip mechanisms is that it does not preserve the normal atomic coordination number. To minimize the increase in energy due to this, the mechanism requires multiple stacking faults to create the total dislocation. Conceptually, there are no issues extending this mechanism to also describe slip on the $\{11\bar{2}1\}\langle 11\bar{2}\bar{6}\rangle$ system.

Due to the fact that this mechanism does not allow for the preservation of the normal atomic coordination number, the energy required for this slip to occur in this way must be significantly larger than on other slip systems. Since the pressures, and hence deformation energies generated using laser shocks have only been recently achieved, this may explain why this type of slip behavior has not been observed frequently. It should be noted that experimental evidence indicating combined slip on $\{11\bar{2}2\}$ and $\{10\bar{1}1\}$ planes in their common $\langle 11\bar{2}\bar{3}\rangle$ direction has been reported[41], although the existence of slip exclusively on $\{11\bar{2}2\}$ planes has not been confirmed.

To answer why <0001> oriented grains deform on the $\{11\bar{2}2\}\langle 11\bar{2}\bar{3}\rangle$ and $\{11\bar{2}1\}\langle 11\bar{2}\bar{6}\rangle$ slip systems, we need to consider the difficulty of deformation, or "hardness", of those grains in deformation to these slip system. This was achieved by the calculation of the Taylor factors[42] of the grains. The calculation was performed for concurrent slip on the $\{11\bar{2}2\}\langle 11\bar{2}\bar{3}\rangle$ and $\{11\bar{2}1\}\langle 11\bar{2}\bar{6}\rangle$ systems activated by an uniaxial compression stress state, with the assumption that the critical resolved shear stress was equal for both slip systems.

Figure 7 shows the calculated Taylor factors for all the grains in the field of view. From this, it can be readily observed that the grains with observed surface slip steps have the lowest Taylor factors. Since

lower Taylor factors indicate easier deformation on the specified slip systems, this then indicates that these grains are ideally oriented if slip was to occur on the $\{11\bar{2}2\}\langle 11\bar{2}\bar{3}\rangle$ and $\{11\bar{2}1\}\langle 11\bar{2}\bar{6}\rangle$ systems due to LSP.

- Lattice Behavior:

While we considered the overall deformation mechanisms in the previous section, we now consider the effect of these different mechanisms on the resultant microstructure. Of interest is the amount of deformation within the grains, which is important because it can elucidate the local distribution of dislocations and hence stresses.

To carry this out, the smaller EBSD scans are used. Calculation of the local average lattice rotation at any point within the grain illustrate where a higher average rotation exists. Higher rotations indicate a local increase in the amount of dislocations and stress. Computationally, this involves determining the average angular misorientation between any given point in the map and all of its six nearest neighbors (since these scans are performed on a triangular grid, each point has 6 nearest neighbor points).

In Figure 8, the resulting lattice rotation map of the region shown in Figure 5(a) for grain 3b is presented. It can be seen that in grain 3b itself, which deformed by slip, the lattice rotations are concentrated on the slip steps. Virtually no lattice rotation is observed between the slip steps. On the other hand in the grain immediately above grain 3b which did not deform by slip, the lattice rotations do not concentrate about any geometric feature and are in general spread throughout the grain.

It can then be deduced then that stress concentrations exist within the <0001> oriented grains, and they are located at the slip steps. These concentrations, combined with the slip step geometry, may consequently be initiation sites for fatigue cracks during cyclic loading. The implication of this then is that fatigue life of LSP treated material may be increased if the amount of <0001> oriented grains is minimized.

V. SUMMARY

In this work, we characterized the surface of a beta solution treated and overaged (BSTOA) Ti-6Al-4V alloy specimen deformed by laser shock processing using electron backscatter diffraction, scanning electron microscopy, and atomic force microscopy. Slip steps were observed within <0001> oriented grains. Analysis of the slip step traces showed that the slip planes were $\{11\bar{2}2\}$ for grains with

their c-axis within 15° of the specimen surface normal and $\{11\bar{2}1\}$ for grains with their c-axis between 15° and 40° away from the specimen surface normal. The slip systems are shown to be the twinning systems $\{11\bar{2}2\}\langle 11\bar{2}\bar{3}\rangle$ and $\{11\bar{2}1\}\langle 11\bar{2}\bar{6}\rangle$ operating in slip. Other grains that do not show slip steps are assumed to deform by deformation twinning. Calculation of the Taylor factors associated with these slip systems shows that the grains with slip steps have the lowest Taylor factor values.

Calculation of localized lattice rotations showed differing behavior in grains with slip steps in comparison to those without. In the grains exhibiting slip steps, all the lattice rotations were concentrated about the steps, with almost no orientation variations in between, indicating that stress concentrations exist at the slip steps. Since these may affect the fatigue performance of the material, it is suggested that minimization of <0001> oriented grains would benefit fatigue life.

It must be mentioned that in this work the specimen was shocked only once, primarily to help understand the deformation mechanisms involved. In typical commercial applications however, at least three or four shock iterations are used. The effect of these repeated shocks on the slip behavior is not yet known, and although it is beyond the scope of this work, a study on this is necessary to understand the evolution of deformation behavior during laser shock processing.

ACKNOWLEDGEMENTS

Chanh Truong is gratefully acknowledged for his work in laser shock treating the specimen. Professor Michael Hill, Dr. Tom Arsenlis, and Dr. Adrian Dewald are acknowledged for insightful and useful discussions. This work was performed under the auspices of the U. S. Department of Energy by the University of California Lawrence Livermore National Laboratory under contract No. W-7405-Eng-48.

REFERENCES

1. G.A. Askar'yan and E.M. Moroz, JETP Lett. **16**, 1638 (1963).
2. F. Neumann, Appl. Phys. Lett. **4**, 167 (1964).
3. D.W. Gregg and S.J. Thomas, J. Appl. Phys. **37**, 2787 (1966).
4. C.H. Skeen and C.M. York, Appl. Phys. Lett. **12**, 369 (1968).
5. N.C. Anderholm, Appl. Phys. Lett. **16**, 113 (1970).
6. S.A. Metz and F.A. Smidt, Jr., Appl. Phys. Lett. **19**, 207 (1971).
7. L.C. Yang and V. J. Menichelli, Appl. Phys. Lett. **19**, 473 (1971).
8. H.J. Hegge and J. Th. M. De Hosson, Acta Metall. Mater. **38**, 2471 (1990).
9. J. Noordhuis and J. Th. M. De Hosson, Acta Metall. Mater. **41**, 1989 (1993).
10. G. Shi, P. Dang, J. Liu, H. Yin, and J. Wang, Acta Metall. Mater. **43**, 217 (1995).
11. J.L. De Mol van Otterloo, D. Bangoli, and J. Th. M. De Hosson, Acta Metall. Mater. **43**, 2649 (1995).
12. P.R. Smith, M.J. Shepard, P.S. Prevéy III, and A.H. Clauer, J. Mat. Eng. Perf. **9**, 33 (2000).
13. M.J. Shepard, P.R. Smith, and M.S. Amer, J. Mat. Eng. Perf. **10**, 670 (2001).
14. A.T. Dewald, J.E. Rankin, M.R. Hill, M.J. Lee, and H. Chen J. Eng. Mat. Tech. **126**, 465 (2004).
15. B.P. Fairland, A.H. Clauer, R.G. Jung, and B.A Wilcox, Appl. Phys. Lett. **25**, 431 (1974).
16. B.P. Fairland and A.H. Clauer, J. Appl. Phys. **50**, 1497 (1979).
17. B.S. Yilbas, S.Z. Shuja, A. Arif, and M.A. Gondal, J. Mat. Proc.Tech. **135**, 6 (2003).
18. T. Thorslund, F. Kahlen, and A. Kar, Optics and Lasers in Eng. **39**, 51 (2003).
19. B.S. Yilbas, A.F.M. Arif, S.Z. Shuja, M.A. Gondal, and J. Shirokof, J. Mat. Eng. Perf. **13**, 47 (2004).
20. B.P. Fairland, B.A. Wilcox, W.J. Gallagher, and D.N. Williams, J. Appl. Phys. **43**, 3893 (1972).
21. G.H. Campbell and M. Kumar, Z. Metallkd. **94**, 3 (2003).
22. M.A. Meyers, F. Gregori, B.K. Kad, M.S. Schneider, D.H. Kalantar, B.A. Remington, G. Ravichandran, T. Boehly, and J.S. Wark, Acta Mat. **51**, 1211 (2003).

23. J. Kaspar and A. Luft, Surf. Eng **17**, 379 (2001).
24. Y. Sano, M. Kimura, N. Mukai, M, Yoda, M. Obata, and T. Ogisu, Proc. SPIE **3888**, 295 (1999).
25. Y. Sano, M. Kimura, K. Sato, M. Obata, A. Sudo, Y. Hamamoto, S. Shima, Y. Ichikawa, H. Yamazaki, M. Naruse, S. Hida, T. Watanabe, and Y. Oono, Proc. ICONE 8, Paper ICONE-8441 (2000).
26. P. Peyre, X. Scherpereel, L. Berthe, C. Carboni, R. Fabbro, G. Béranger, and C. Lemaitre, Mat. Sci. Eng. A **280**, 294 (2000).
27. H. Zhang, Y.-K. Zhang, and C.-Y. Yu, Surf. Eng. **15**, 454 (1999).
28. J.J. Ruschau, R. John, S.R. Thompson, and T. Nicholas, Intl. J. Fatigue **21**, S199 (1999).
29. C.S. Montross, T. Wei, L. Ye, G. Clark, and Y. Mai, Intl. J. Fatigue **24**, 1021 (2002).
30. C.A. Radopoulos, J.S. Romero, S.A. Curtis, E.R. de los Rios, and P. Peyre, J. Mat. Eng. Perf. **12**, 414 (2003).
31. R.K. Nalla, I. Altenberger, U. Noster, G.Y. Liu, B. Scholtes, and R.O. Ritchie, Mat. Sci. Eng. A **355**, 216 (2003).
32. Y.Lii, V.Ramachandran, and R.E. Reed-Hill, Metall. Trans , **1**, 447 (1970).
33. S.I. Wright and B.L. Adams, Metall. Trans. A, **23A**, 759 (1992).
34. B.L. Adams, S.I. Wright and K. Kunze, Metall. Trans A, **24A**, 819 (1993).
35. A. Morawiec, J. Appl. Cryst,. **31**, 818, (1998).
36. F.D. Rosi, C.A.Dube, and B.H. Alexander, Trans AIME **197**, 257 (1953).
37. E.A.Anderson, D.C. Jillson, and S.R. Dunar, Trans AIME **197**, 1191 (1953).
38. E.J. Rapperport, and C.S Hartley, Trans AIME **218**, 869 (1960).
39. P.G. Partridge and C.J. Peel, in *The Science, Technology, and Application of Titanium*, R.I. Jaffee and N.E. Promisel eds,517, (1970).
40. H.S. Rosenbaum, in *Deformation Twinning*, R.E. Reed-Hill, J.P. Hirth, and H. C. Rogers eds, **25**, 43 (1964).
41. J.C. Williams and M.J. Blackburn, Phys. Stat. Sol., **25**, K1 (1968).
42. G.I. Taylor, *J. Inst. Met.*, **62**, 307 (1938).

FIGURE CAPTIONS

Table I. Slip planes of steps observed on identified grains.

Figure 1. Schematic of specimen surface showing area examined in this study.

Figure 2. Schematic of laser shock process.

Figure 3. Large area microstructure maps obtained using (a) EBSD showing grain boundaries in black, and (b) 540 SEM backscatter electron images showing topographic variation. Grains with observable slip steps are identified in (a), and those identified with the same number but different letter are related to each other by a small rotation ($<10^{o}$).

Figure 4. (a) Slip steps observed on grains 2a and 2b displayed as the EBSD map grain boundaries overlaid on an SEM map section obtain from Fig. 2. (b) 100μm x 100μm AFM topographic map of boxed region in Fig. 4(a), with vectors n_1, n_2, and n_3 representing the slip trace normals. (c) Stereographic projection of crystallographic plane normals of known α-titanium slip planes in grain 2b, showing that $\{11\bar{2}2\}$ planes are the slip planes. Great circles are used to represent the slip trace normals. (d) Schematic of crystallographic plane traces parallel to slip steps in Fig. 3(b) identified using orientation information obtained from EBSD.

Figure 5. (a) 80μm x 80μm topographic AFM map of Grain 3b with vectors n_1 and n_2 representing the slip trace normals. (b) Stereographic projection of crystallographic plane normals of known α-titanium slip planes in grain 3b, showing that none of them are the slip planes in this grain. The slip planes were determined to be $\{11\bar{2}1\}$. Great circles are used to represent the slip trace normals.

Figure 6. Inverse pole figure showing crystallographic plane normals parallel to specimen surface normal for (a) all grains with observed surface slip steps, (b) grains with $\{11\bar{2}2\}$ slip plane traces, and (c) grains with $\{11\bar{2}1\}$ slip plane traces. Values are multiple times random.

Figure 7. Taylor factor calculation for $\{11\bar{2}2\}\langle 11\bar{2}\bar{3}\rangle$ and $\{11\bar{2}1\}\langle 11\bar{2}\bar{6}\rangle$ slip systems for all the grains in the region studied, with grain boundaries shown as white. Grain numbers are the same as used in Figure 3(a). It can be seen that in general, the Taylor factor is lower for the grains with slip steps.

Figure 8. EBSD map of area shown in Figure 5(a) for grain 3b. Grayscale values represent average nearest neighbor misorientation as a function of location. Grain boundaries are shown as white lines. In the grains with slip steps, lattice rotation peaks are seen at the slip steps, but not in the regions between. In the grain with no slip steps, lattice rotation peaks are distributed throughout.

Table I. Slip planes of steps observed on identified grains.

Grain ID	Observed Slip Plane
1a	$\{11\bar{2}2\}$
1b	$\{11\bar{2}2\}$
2a	$\{11\bar{2}2\}$
2b	$\{11\bar{2}2\}$
3a	$\{11\bar{2}1\}$
3b	$\{11\bar{2}1\}$
4	$\{11\bar{2}1\}$
5	$\{11\bar{2}1\}$
6	$\{11\bar{2}2\}$
7	$\{11\bar{2}2\}$
8	$\{11\bar{2}2\}$
9	$\{11\bar{2}2\}$
10	$\{11\bar{2}2\}$

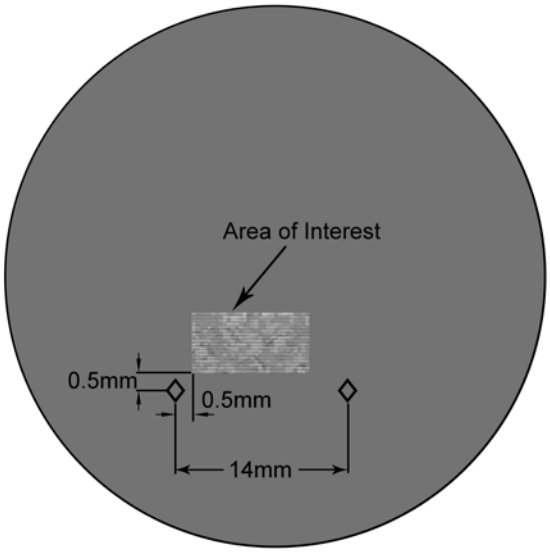

Figure 1. Schematic of specimen surface showing area examined in this study.

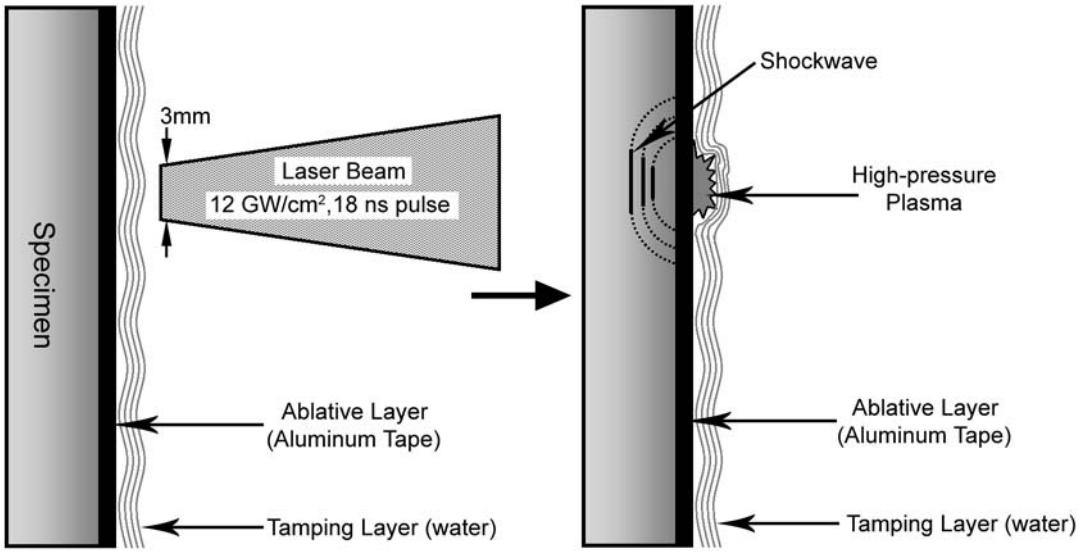

Figure 2. Schematic of laser shock process.

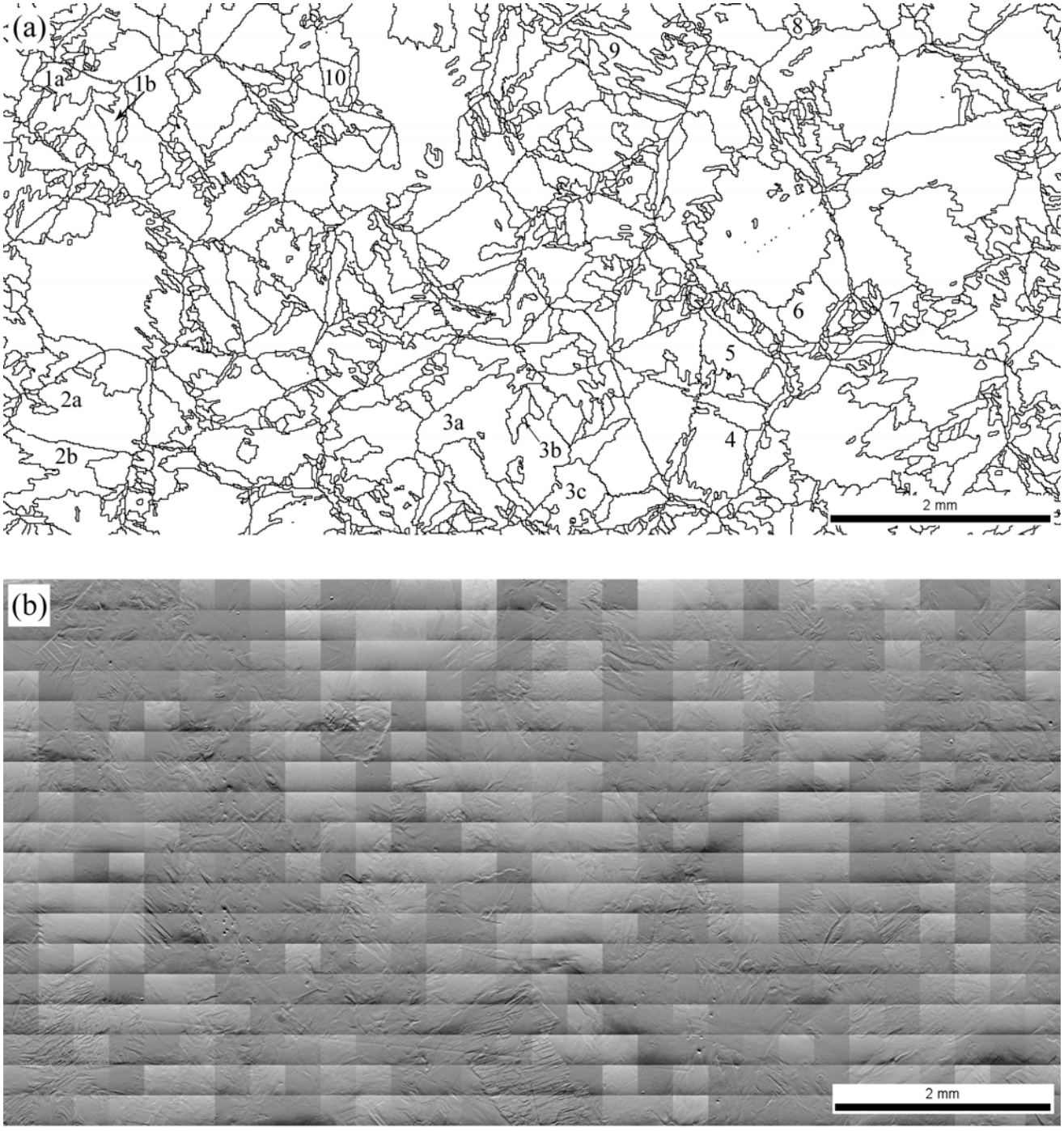

Figure 3. **Large area microstructure maps obtained using (a) EBSD showing grain boundaries in black, and (b) 540 SEM backscatter electron images showing topographic variation. Grains with observable slip steps are identified in (a), and those identified with the same number but different letter are related to each other by a small rotation (<10^{o}).**

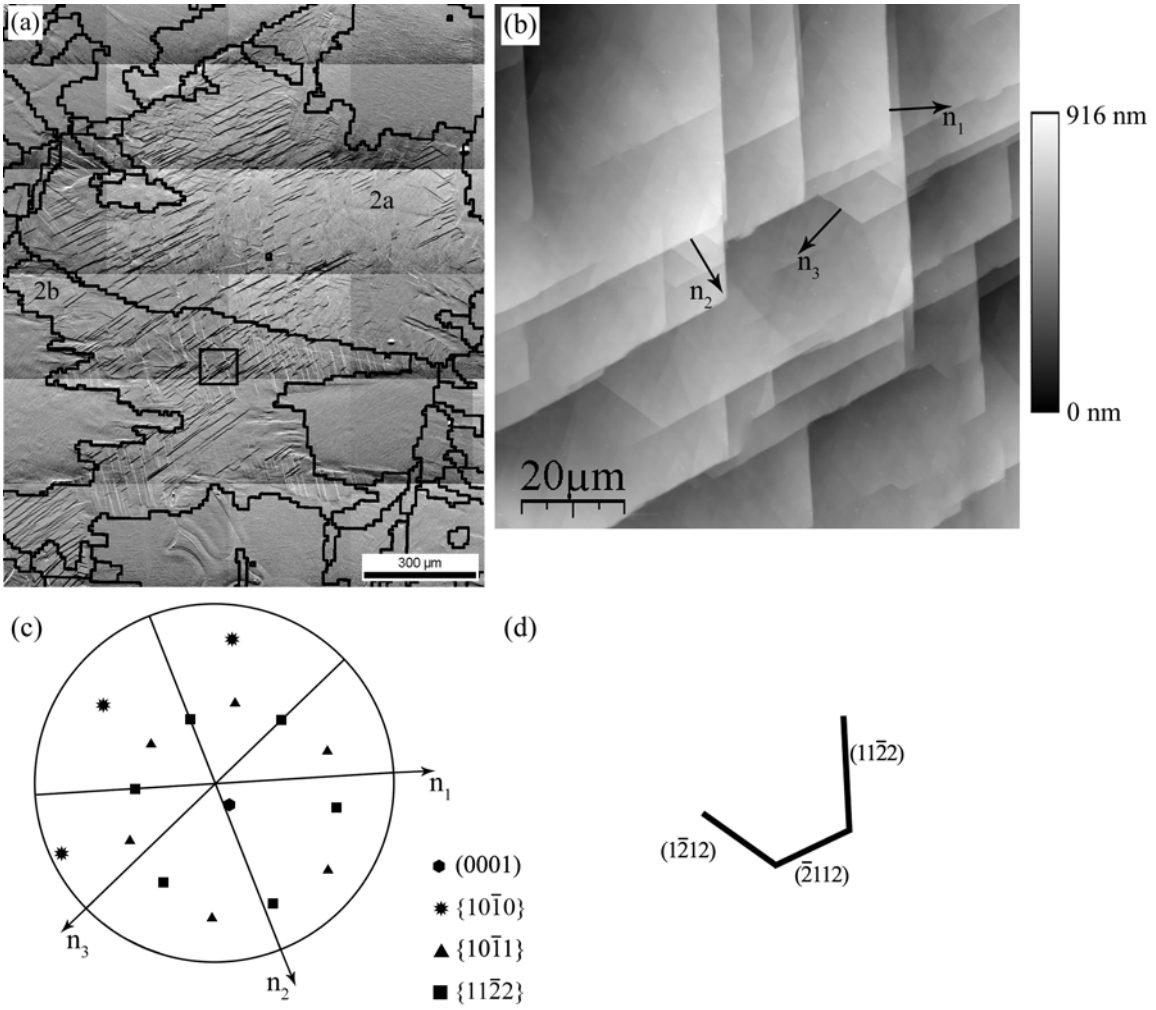

Figure 4. **(a) Slip steps observed on grains 2a and 2b displayed as the EBSD map grain boundaries overlaid on an SEM map section obtain from Fig. 2. (b) 100µm x 100µm AFM topographic map of boxed region in Fig. 4(a), with vectors n_1, n_2, and n_3 representing the slip trace normals. (c) Stereographic projection of crystallographic plane normals of known α-titanium slip planes in grain 2b, showing that $\{11\bar{2}2\}$ planes are the slip planes. Great circles are used to represent the slip trace normals. (d) Schematic of crystallographic plane traces parallel to slip steps in Fig. 3(b) identified using orientation information obtained from EBSD.**

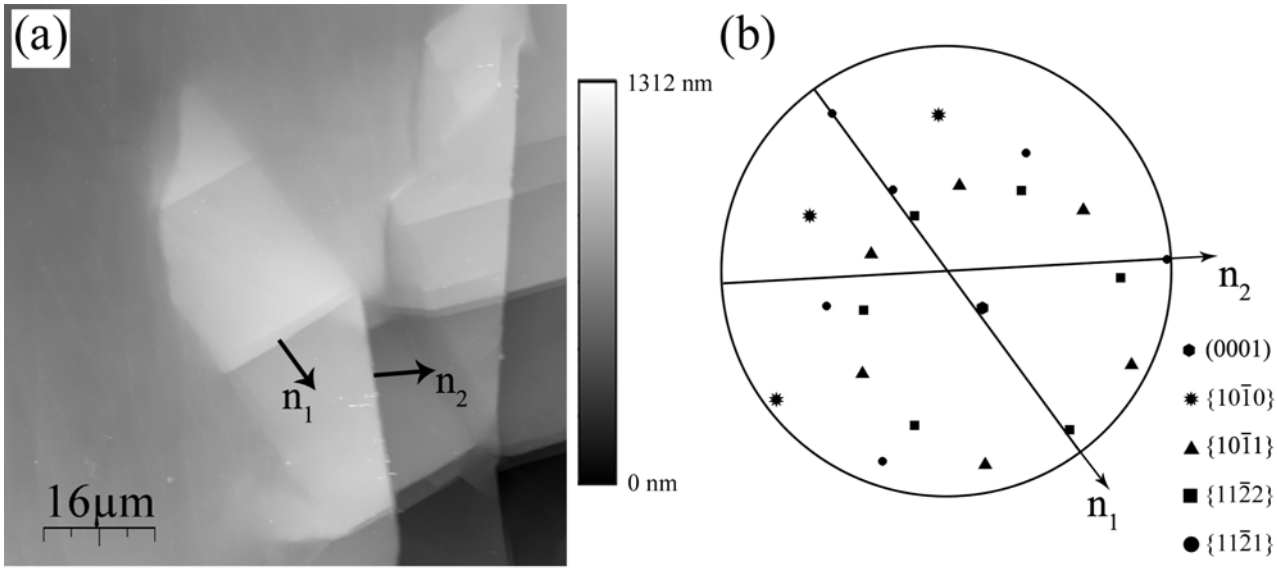

Figure 5. **(a) 80μm x 80μm topographic AFM map of Grain 3b with vectors n_1 and n_2 representing the slip trace normals. (b) Stereographic projection of crystallographic plane normals of known α-titanium slip planes in grain 3b, showing that none of them are the slip planes in this grain. The slip planes were determined to be $\{11\bar{2}1\}$. Great circles are used to represent the slip trace normals.**

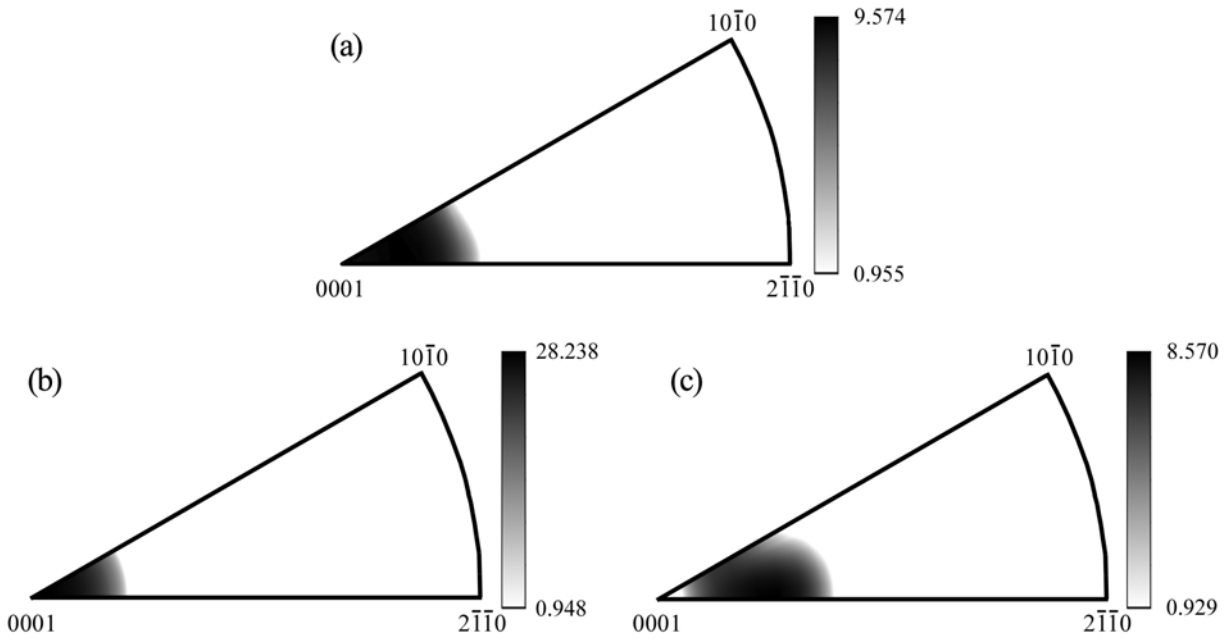

Figure 6. **Inverse pole figure showing crystallographic plane normals parallel to specimen surface normal for (a) all grains with observed surface slip steps, (b) grains with $\{11\bar{2}2\}$ slip plane traces, and (c) grains with $\{11\bar{2}1\}$ slip plane traces. Values are multiple times random.**

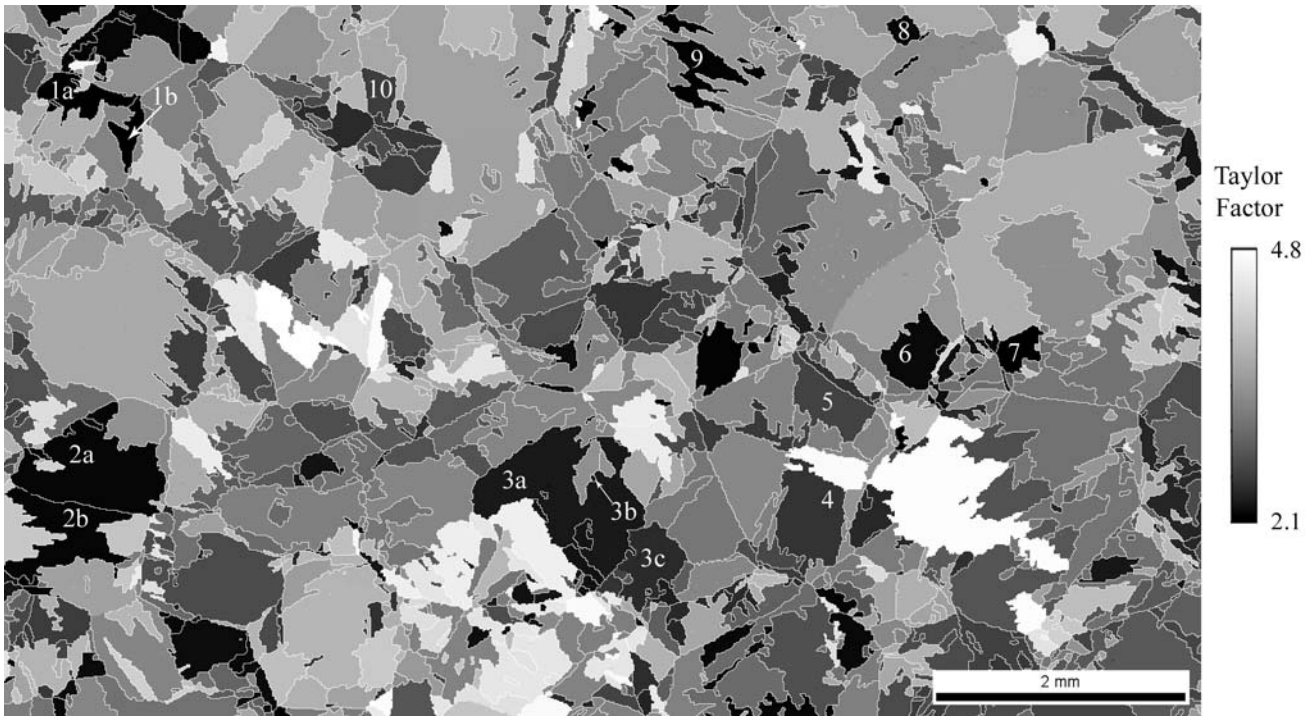

Figure 7. **Taylor factor calculation for $\{11\bar{2}2\}\langle 11\bar{2}\bar{3}\rangle$ and $\{11\bar{2}1\}\langle 11\bar{2}\bar{6}\rangle$ slip systems for all the grains in the region studied, with grain boundaries shown as white. Grain numbers are the same as used in Figure 3(a). It can be seen that in general, the Taylor factor is lower for the grains with slip steps.**

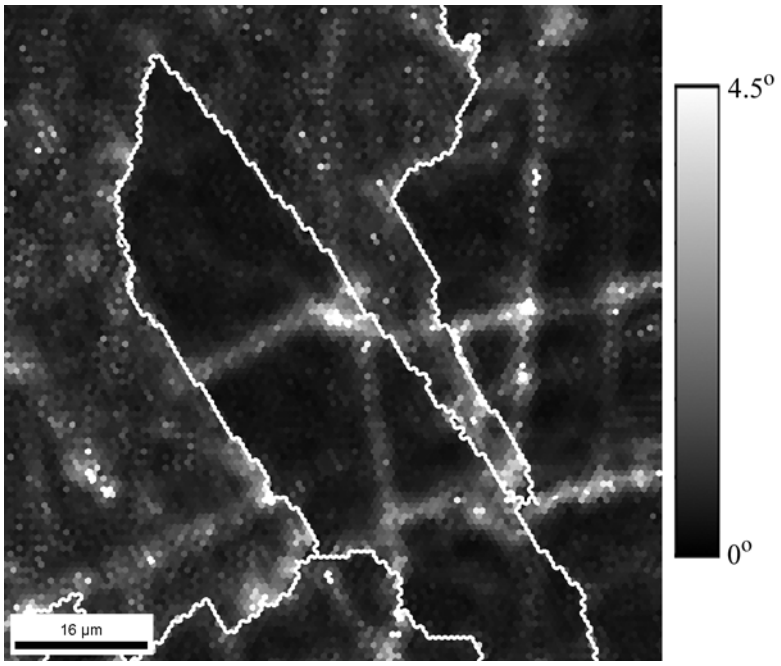

Figure 8. **EBSD map of area shown in Figure 5(a) for grain 3b. Grayscale values represent average nearest neighbor misorientation as a function of location. Grain boundaries are shown as white lines. In the grains with slip steps, lattice rotation peaks are seen at the slip steps, but not in the regions between. In the grain with no slip steps, lattice rotation peaks are distributed throughout.**

Grain ID	Observed Slip Plane
1a	$\{11\bar{2}2\}$
1b	$\{11\bar{2}2\}$
2a	$\{11\bar{2}2\}$
2b	$\{11\bar{2}2\}$
3a	$\{11\bar{2}1\}$
3b	$\{11\bar{2}1\}$
4	$\{11\bar{2}1\}$
5	$\{11\bar{2}1\}$
6	$\{11\bar{2}2\}$
7	$\{11\bar{2}2\}$
8	$\{11\bar{2}2\}$
9	$\{11\bar{2}2\}$
10	$\{11\bar{2}2\}$

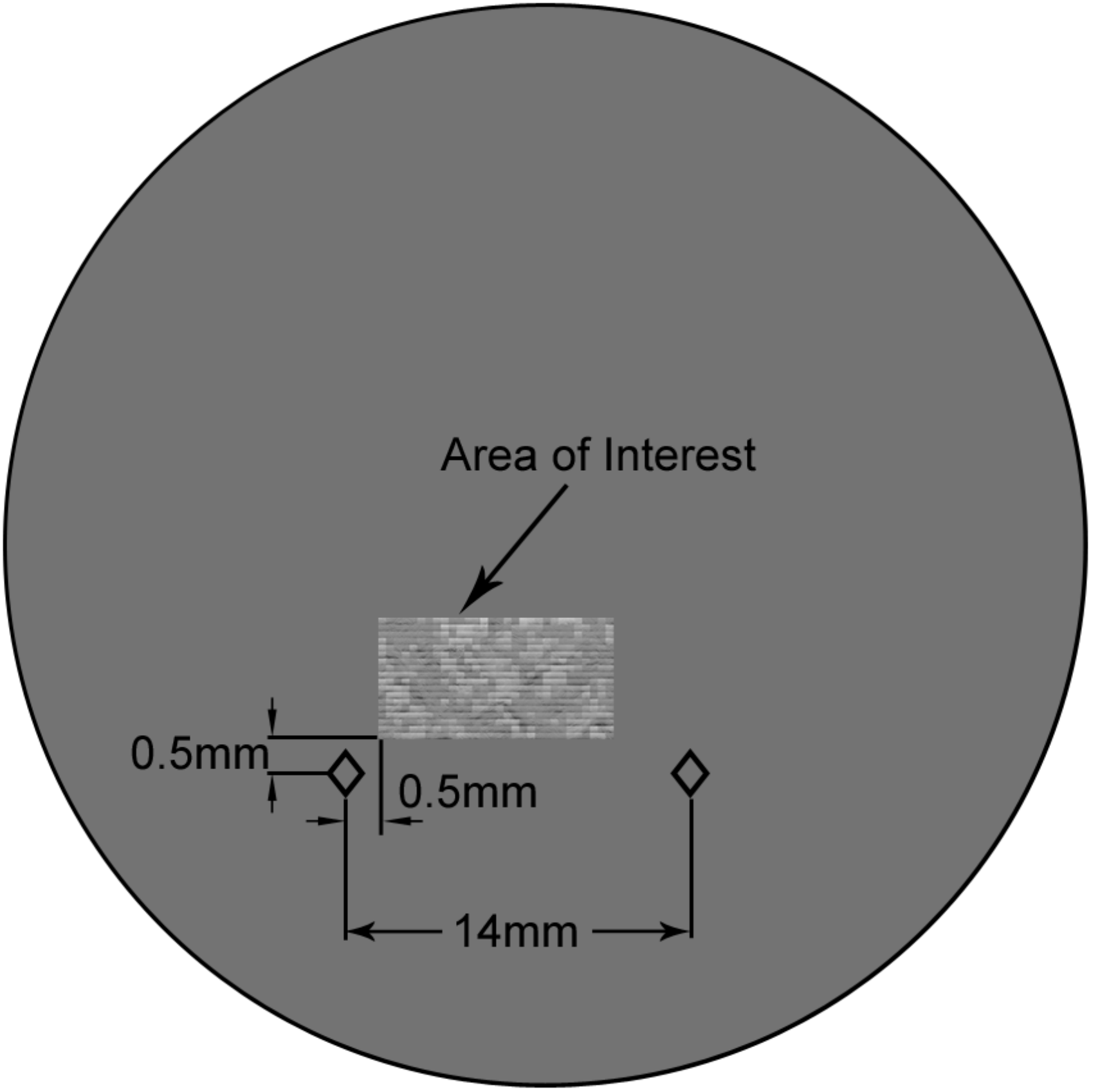
Area of Interest
0.5mm
0.5mm
14mm

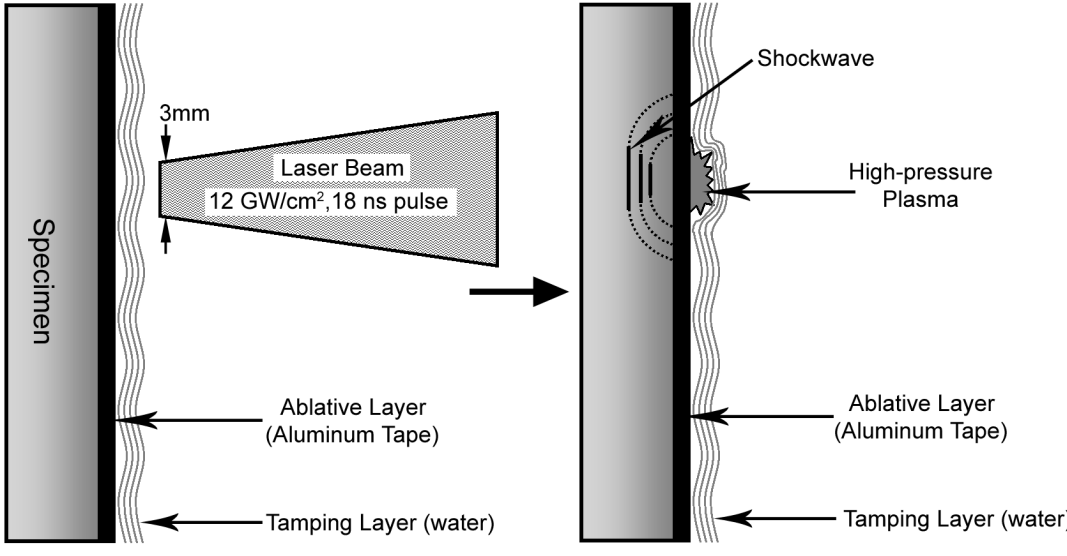
Specimen
3mm
Laser Beam
12 GW/cm2,18 ns pulse
Ablative Layer
(Aluminum Tape)
Tamping Layer (water)
Shockwave
High-pressure
Plasma
Ablative Layer
(Aluminum Tape)
Tamping Layer (water)

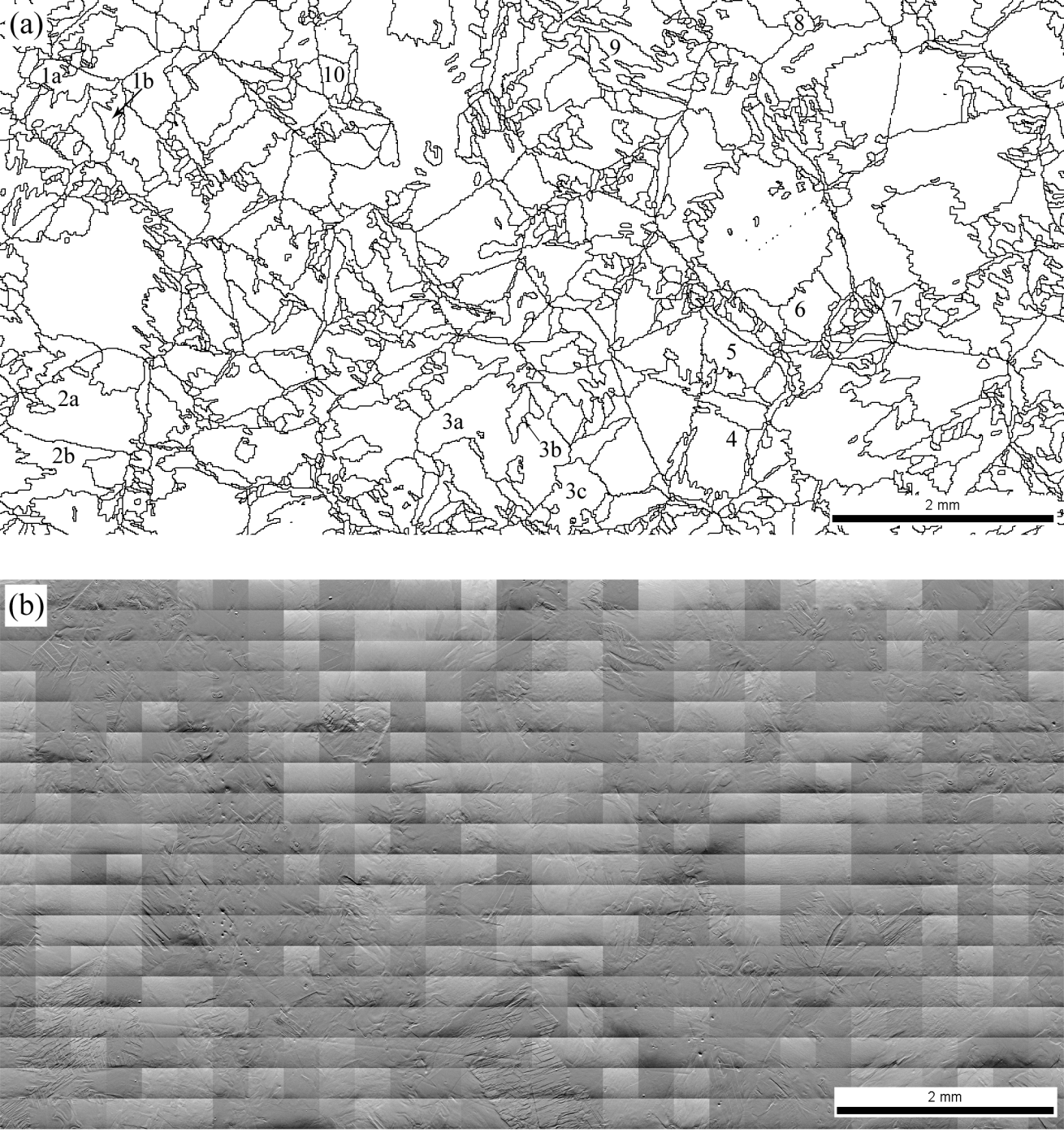
(a)
1a
1b
10
9
8
6
7
5
4
2a
2b
3a
3b
3c
2 mm
(b)
2 mm

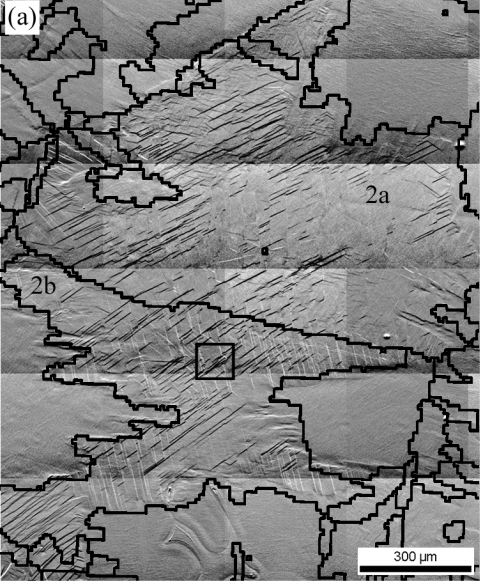
(a)
2a
2b
300 μm

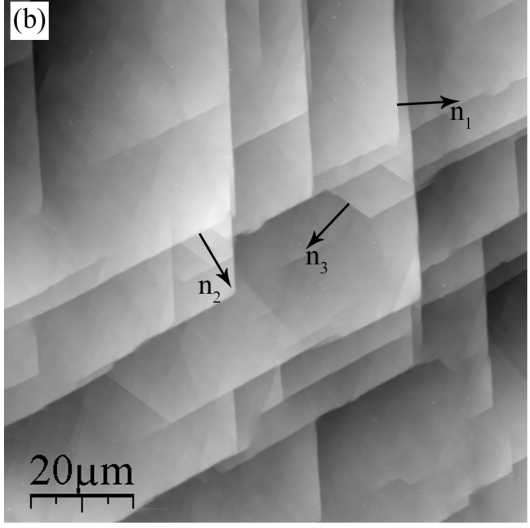
(b)
n1
n2
n3
916 nm
0 nm
20μm

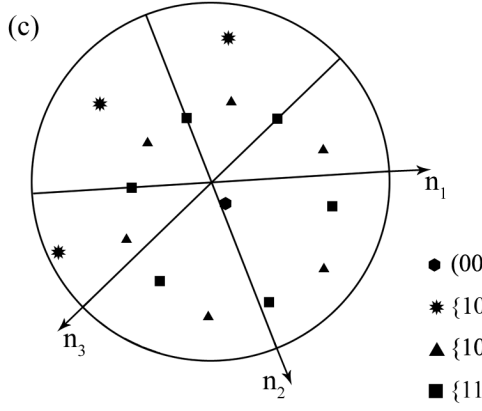
(c)
n1
n2
n3
(0001)
{10$\bar{1}$0}
{10$\bar{1}$1}
{11$\bar{2}$2}

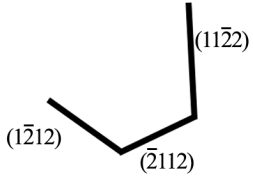
(d)
(11$\bar{2}$2)
(1$\bar{2}$12)
($\bar{2}$112)

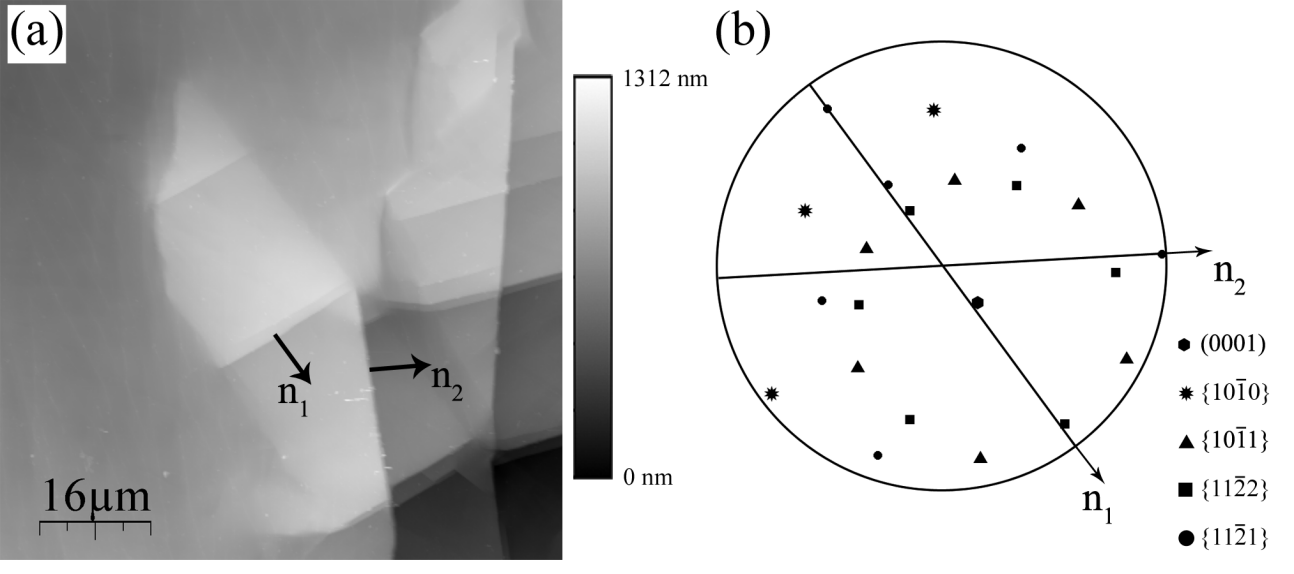
(a)
1312 nm
0 nm
n1
n2
16μm
(b)
n2
n1
(0001)
{10$\bar{1}$0}
{10$\bar{1}$1}
{11$\bar{2}$2}
{11$\bar{2}$1}

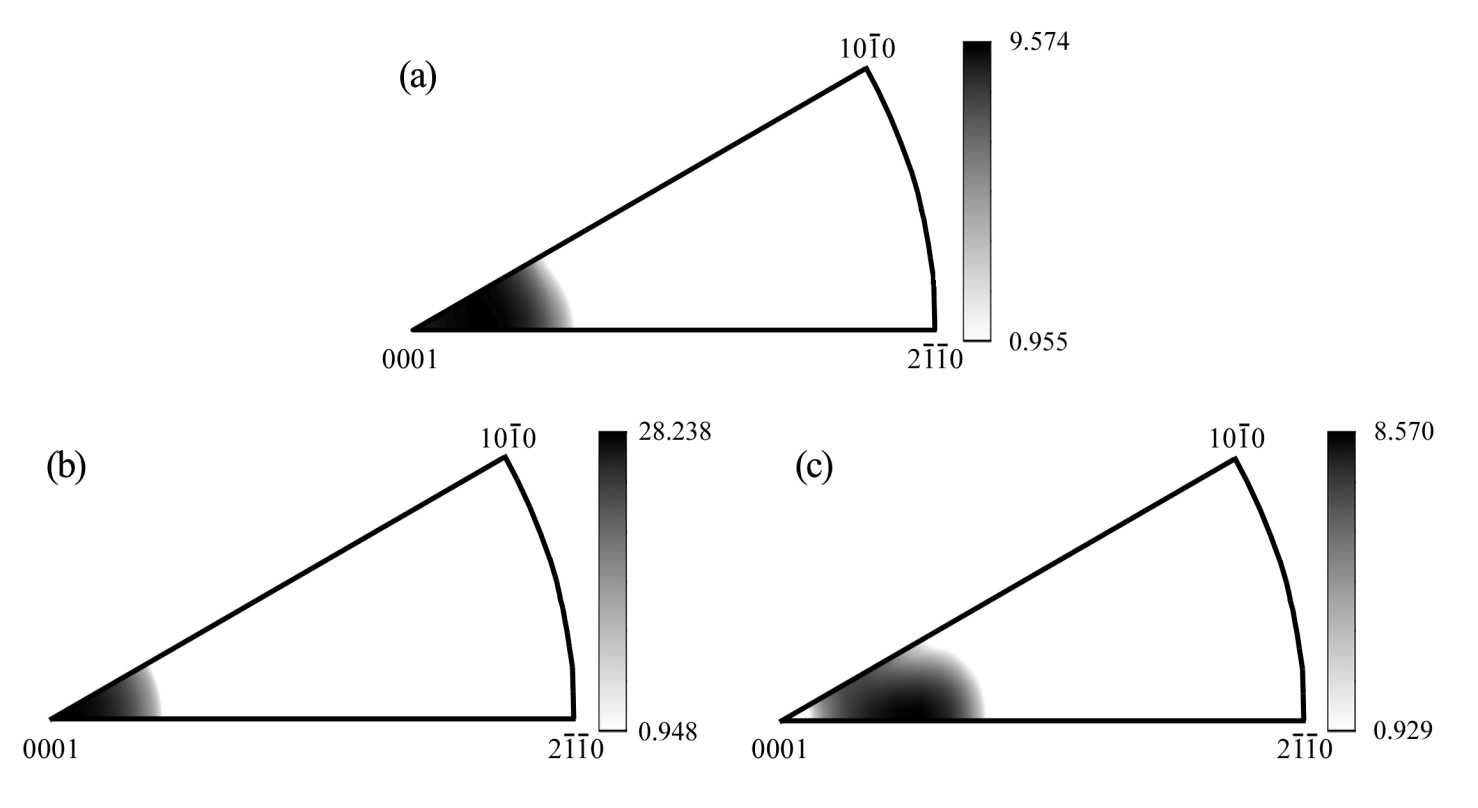
(a)
$10\bar{1}0$
9.574
0.955
0001
$2\bar{1}\bar{1}0$
(b)
$10\bar{1}0$
28.238
0.948
0001
$2\bar{1}\bar{1}0$
(c)
$10\bar{1}0$
8.570
0.929
0001
$2\bar{1}\bar{1}0$

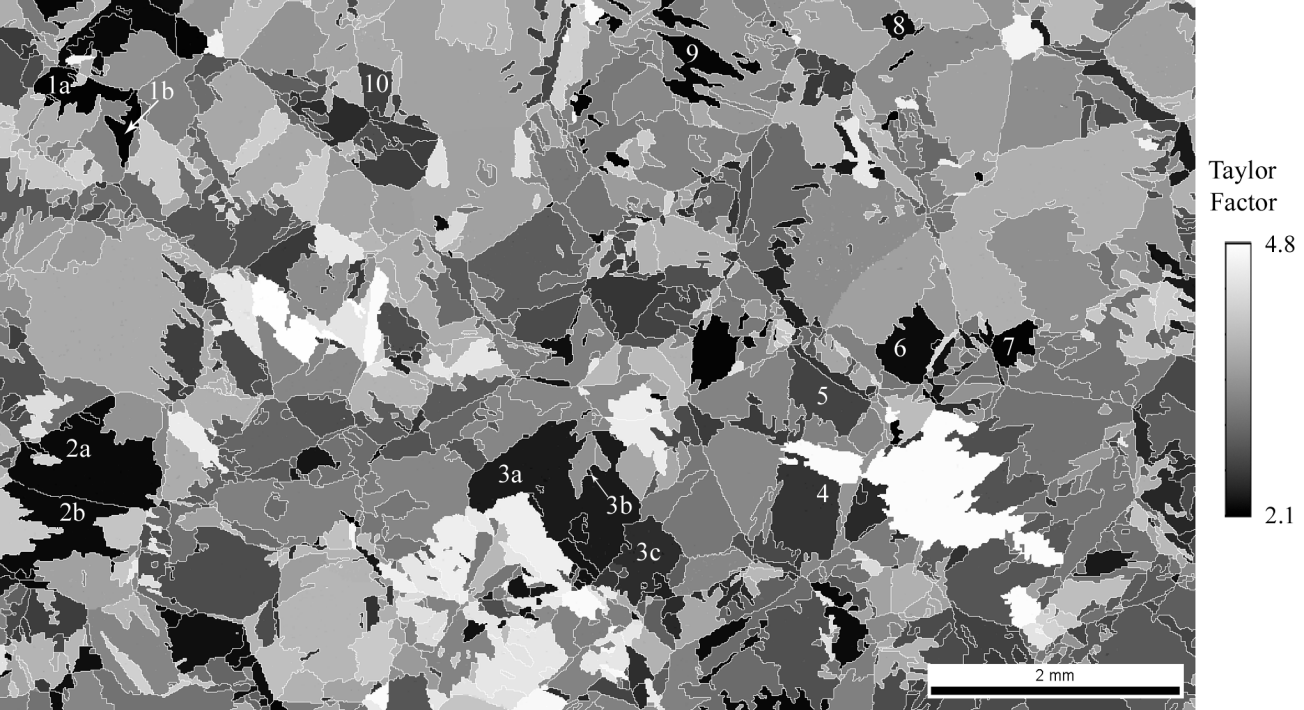
1a
1b
10
9
8
6
7
5
2a
2b
3a
3b
3c
4
Taylor Factor
4.8
2.1
2 mm

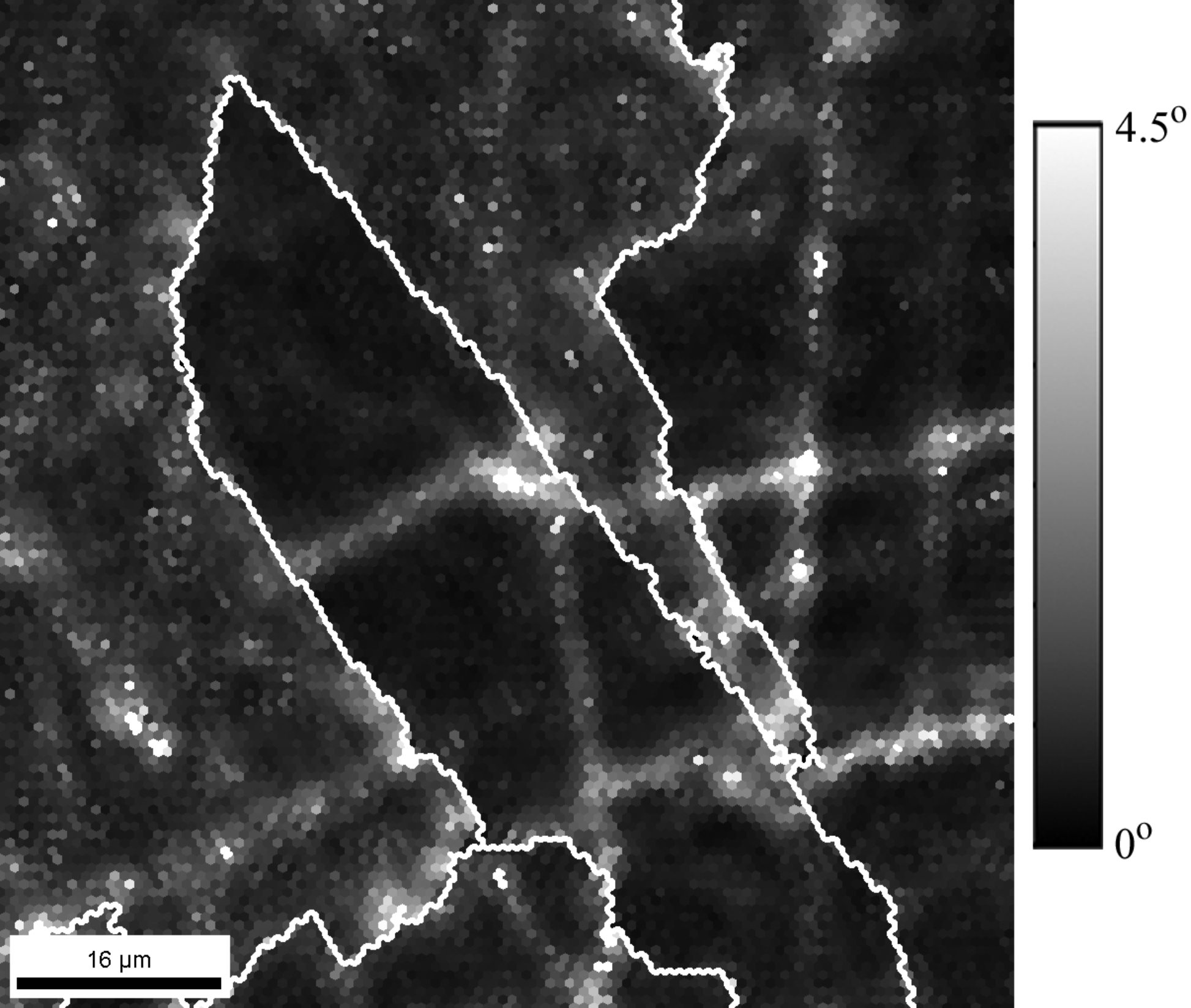
4.5°
0°
16 µm